

PAPER

# Optical emission self-actinometry for measuring absolute number densities of air species diffusing into a helium atmospheric pressure plasma jet

To cite this article: Tam Nguyen *et al* 2021 *J. Phys. D: Appl. Phys.* **54** 405203

View the [article online](#) for updates and enhancements.



**IOP | ebooks™**

Bringing together innovative digital publishing with leading authors from the global scientific community.

Start exploring the collection—download the first chapter of every title for free.

# Optical emission self-actinometry for measuring absolute number densities of air species diffusing into a helium atmospheric pressure plasma jet

Tam Nguyen, Peng Lin, Demetre J Economou\* and Vincent M Donnelly\* 

Plasma Processing Laboratory, Department of Chemical and Biomolecular Engineering, University of Houston, Houston, TX 77204, United States of America

E-mail: [Economou@uh.edu](mailto:Economou@uh.edu) and [vmdonnelly@uh.edu](mailto:vmdonnelly@uh.edu)

Received 16 April 2021, revised 15 June 2021

Accepted for publication 1 July 2021

Published 22 July 2021



CrossMark

## Abstract

Optical emission spectroscopy was used to measure the radial distribution of the mole fraction of ambient air species (Ar, O<sub>2</sub> and N<sub>2</sub>) diffusing into a radio frequency (13.7 MHz) helium (2.0 standard liters per min (slm)), atmospheric pressure plasma jet (APPJ). Line-integrated emissions recorded as a function of lateral position (at fixed axial positions), perpendicular to the jet axis, were magnified and fed into a spectrometer. Selected emission intensities were then Abel inverted to obtain radial emission profiles. The latter were converted into absolute mole fraction profiles, using a ‘self-actinometry’ method, in which known small amounts of Ar, O<sub>2</sub>, or N<sub>2</sub> were added to the He feed gas to produce a small change in emission intensity. Without shielding gas, the on-axis air mole fraction increased from zero at 1 mm, to 10<sup>-3</sup> at 3 mm and 10<sup>-2</sup> at 5 mm from the nozzle. The radial distribution was center-low near the nozzle, and flattened further downstream. N<sub>2</sub> shielding gas (4.5 slm) flow in an annular jet coaxial with the He jet, reduced air diffusion by 2–3 times. Simulation of air diffusion into the plasma jet showed similar axial number densities of air species, as well as similar effectiveness of the shielding gas, compared to experimental data. The shielding effectiveness in this study was lower than that in published works because of the higher gas temperature in the present APPJ.

Keywords: atmospheric pressure plasma, optical emission, shielding gas, Abel inversion

(Some figures may appear in colour only in the online journal)

## 1. Introduction

Atmospheric pressure plasma jets (APPJs) are widely studied mainly for current and potential medical applications [1–4]. The plasma is operated by flowing He or Ar gas through a (usually quartz) capillary tube, with power delivered through a pair of electrodes. The electrodes can take various forms to prevent arcing or to reduce plasma gas temperature [5]. The APPJ can operate in open air, producing a small ‘plasma

needle’, making it suitable for precise, direct treatment of surfaces.

During operation, ambient air diffuses into the plasma jet, producing various reactive oxygen-nitrogen species (RONS) [6–8] that are thought to be beneficial in medical treatments, while often being unwanted for other applications. Furthermore, it is essential to control the RONS species and their concentrations. Reliance on ambient air to produce RONS can lead to inconsistent performance due to the day-to-day changes in atmospheric pressure and humidity. In addition, the N<sub>2</sub>-to-O<sub>2</sub> ratio is limited to that of ambient air. To provide a more controlled environment, ‘shielding’ gas is flown in

\* Authors to whom any correspondence should be addressed.

an annular space coaxial with the jet. This acts as a curtain to separate the plasma from ambient air [9, 10]. Dünbier *et al* [11] used molecular beam mass spectrometry to measure the ambient air species densities, showing controllable behavior by using a shielding gas. Reuter *et al* [10] reported that the nitrite and nitrate amounts produced by a plasma jet were greatly affected in the presence of a shielding gas. Different shielding gases can also be used to control the species generated in the plasma [12–14]. Schmidt-Bleker *et al* [13] demonstrated that increasing the humidity of a mixed oxygen-nitrogen shielding gas decreased the ozone production rate, while increasing the amount of oxygen in the shielding gas increased the ozone production rate. Narimisa *et al* [15] observed that argon shielding gas could improve the degree of wettability of a treated surface and increased the treated area on the substrate compared to nitrogen shielding gas. For a plasma jet in contact with a liquid surface, employing nitrogen shielding gas resulted in more DNA double-strand breaks in cancer cells compared to oxygen shielding gas, indicating the importance of RNS in the liquid [16]. Ogawa *et al* [17] found that using shielding gas increased the length of laminar flow downstream of the nozzle. As a result of the absence of turbulence, the plasma jet footprint on the substrate was minimized [17]. With oxygen-containing shielding gas, negative ions formed mixing layer lowered the plasma conductivity, which led to greater penetration of the electric field [18]. Furthermore it was found that the shielding gas guiding the working gas flow could inhibit flash-overs to the grounded electrode [19].

Most published experimental studies of the chemistry of atmospheric pressure plasmas have focused on identifying reactive species and determining their concentrations. Methods including laser induced fluorescence (both single and two-photon) and optical absorption spectrometry have been used to detect O [20], OH [21, 22], and NO [23, 24]. It is also informative to quantify the concentrations of N<sub>2</sub> and O<sub>2</sub> present in the plasma, as well as Ar (a convenient ‘tracer’ gas in air) in He carrier gas plasmas. These species are not easily detectable by laser induced fluorescence methods (for example, N<sub>2</sub> can be detected by a five-photon process [25], while Ar detection requires three photons for excitation [26]), and does not absorb throughout the ultraviolet to infrared. O<sub>2</sub> absorption at the edge of the vacuum UV is weak and of course interfered with by the surrounding air. Coherent anti-Stokes Raman spectroscopy (CARS) has been used to detect N<sub>2</sub> in atmospheric pressure plasmas [27], however, CARS is less sensitive than other methods for detecting trace species. In addition, CARS is not easily applicable for spatially resolved measurement, due to the need to simultaneously move the pump beams and signal beam [27].

Previously, we reported a ‘self-actinometry’ method that can be used to obtain absolute number densities of stable species in low pressure plasmas. N<sub>2</sub> and CO number densities were obtained in NH<sub>3</sub> and CH<sub>3</sub>F/O<sub>2</sub> plasmas [28, 29], respectively, and were verified by independent spectroscopic measurements. In this study, self-actinometry was demonstrated under the more complex conditions encountered in atmospheric pressure plasmas. Radial distribution of absolute number densities were obtained for air species diffusing into

the plasma jet with or without a shielding gas. The radial emission profiles of these species were obtained first, and then converted into radial mole fraction profiles. The experimental data were compared with simulation predictions.

## 2. Experimental methods

### 2.1. Plasma jet configuration and collection of emission

A helium plasma jet (figure 1) was made by flowing 2 standard liters per minute (slm) He (ultra high purity, with typical impurity levels of <0.1 ppm Ar [30], <4 ppm O<sub>2</sub> and <5 ppm water) through a central quartz tube (2 mm inner diameter). A grounded copper ring was wrapped around the central tube. A tungsten needle electrode inside the tube was powered with a 13.7 MHz, 1.7 kV peak-to-peak sinewave voltage supplied by a function generator and amplifier. The amplifier output was connected to one end of a coil. The other end of the coil was connected to the tungsten needle electrode. The design of the plasma source and configuration of the matching network coil were as described by Bruggeman *et al* [31], with small modifications to dimensions and operating frequency. The applied frequency was tuned to minimize reflected power to less than a few W with 40 W forward power measured with a Bird power meter between the amplifier output and matching network input. This measurement does not account for any power lost in the matching network and thus somewhat overestimates the true power dissipated in the discharge.

Superimposed on the schematic in figure 1 is a white light photograph of the plasma jet. Visible emission from the jet extends to a distance of about 7 mm from the nozzle. With the plasma source axis oriented in the horizontal direction, light perpendicular to the axis of the plasma jet was magnified by a lens (15 cm focal length, 4× magnification, with an 8 mm diam. aperture) and focused onto a 0.5 mm core optical fiber, thus providing a spatial resolution of 0.125 mm (figure 2). By moving the optical fiber in the vertical direction, perpendicular to the jet axis at a fixed axial position, the laterally resolved emission was captured and fed into a spectrometer consisting of a 0.55 m focal length monochromator (ISA model TRIAX 550) and an intensified charge-coupled device (ICCD, Princeton Instruments, model PI-Max I). The grating used was 300 grooves mm<sup>-1</sup>, producing a resolution of 1 nm for a 0.4 mm slit width, sufficient to resolve the emission lines and bands of interest. While the ICCD is capable of providing time-resolved measurements, signals were collected over many cycles of applied voltage and thus provided time-averaged values. This also averages-out any fluctuations in the spatial position of the jet.

The gas temperature was measured by recording the N<sub>2</sub> (C<sup>3</sup>Π<sub>u</sub>, v' = 0 → B<sup>3</sup>Π<sub>g</sub>, v'' = 2) vibronic emission band near 380 nm, at a distance of 5 mm from the nozzle, with and without shielding gas. The shape of the emission band was simulated and matched to experiments, with the rotational temperature being the only adjustable parameter [32–34]. Temperature was 1000 K without shielding gas and 800 K with shielding gas.

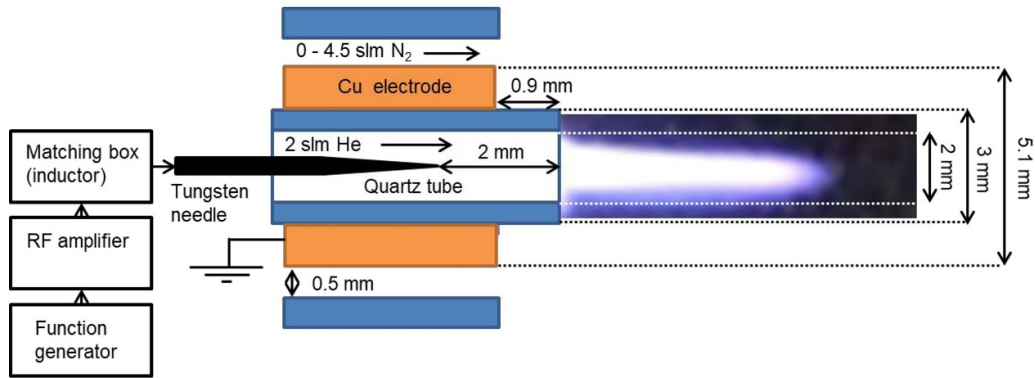


**Figure 1.** RF atmospheric pressure plasma jet configuration. The nitrogen shielding gas flow was either 4.5 slm or zero (no shielding gas).

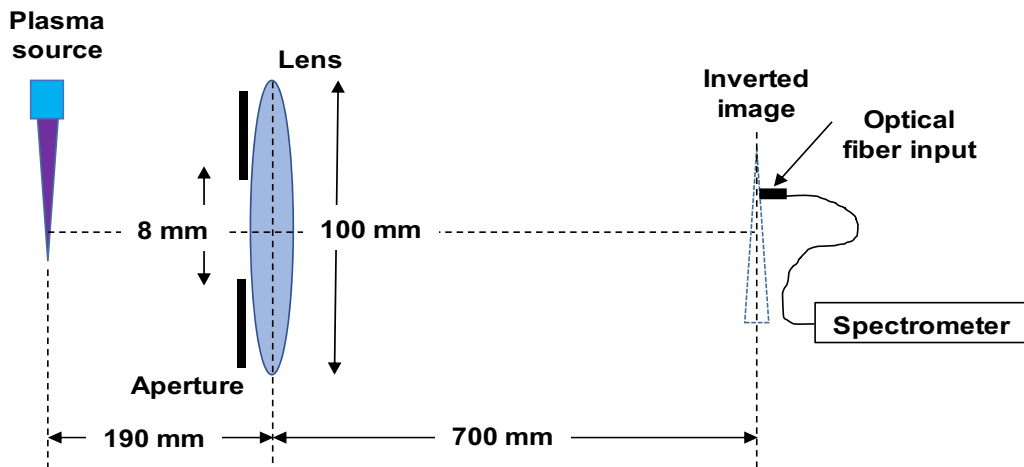


**Figure 2.** Schematic (not drawn to scale) of elements and configuration for collection of APPJ emission.

Using a gas temperature of 900 K, the Reynolds number was  $Re = 90$  at the tip of nozzle of the glass tube where the jet emerged into open air, thus flow was laminar. A co-axial flow of 4.5 slm  $N_2$  shielding gas surrounded the He flow in some experiments, to separate the plasma jet from ambient air, while in other experiments, no shielding gas was used. Mass flow controllers were used to regulate He plasma gas and  $N_2$  shielding gas flow rates. Traces of either Ar,  $O_2$ , or  $N_2$  were also added to the He flow. In this case, a 2 sccm full scale mass flow controller was used. With 2 slm He flow, the regulated trace flow produced mole fractions of between 0.00005 and 0.001.

Emission was Abel inverted (assuming 2D azimuthally symmetric profiles) to produce the radially resolved emission of the plasma jet at different axial positions (1 mm, 3 mm, and 5 mm distance from the nozzle), with or without a 4.5 slm  $N_2$  shielding gas. The Abel inversion was carried out by numerically integrating the expression,

$$f(r) = -\frac{1}{r} \int_r^\infty \frac{dF}{dy} \frac{dy}{\sqrt{y^2 - r^2}}$$

where  $r$  is the radial distance,  $f(r)$  is the radial distribution (derived profile),  $y$  is the lateral distance, and  $F(y)$  is the lateral

distribution (measured profile). This method for acquiring the radial emission intensity was verified by illuminating a thin metal mesh sheet rolled into a 1 mm diam. hollow cylinder, thus creating a light scattering source similar to a hollow, cylindrical emission from air species at the edge of a He plasma jet. Using the same optics as in the experiments, the inverted intensity of the scattered light was sharply peaked at 0.5 mm from the center. The profile fell to zero intensity at the center and at the edge. The Abel inversion was as expected, thus validating the procedure.

### 3. Results and discussion

#### 3.1. Line-integrated radial emission profiles

Line-integrated emission intensities perpendicular to the plasma jet axis were recorded from He ( $3^3S \rightarrow 2^3p^o$ , 706.6 nm), Ar ( $4p\ 2\ [5/2] \rightarrow 4p\ 2\ [3/2]^o$ , 811 nm), O-atom ( $3^5P \rightarrow 3^5S^o$ , 777.5 nm), and  $N_2$  ( $C^3\Pi_u, v' = 0 \rightarrow B^3\Pi_g, v'' = 0$ , 337 nm monitored at 2nd order) as a function of distance from the axis of the cylindrically symmetric plasma for fixed axial distances of 1, 3 and 5 mm from the nozzle. One set of measurements is shown in figure 3, for emission recorded at a fixed axial distance of 5 mm from the nozzle. The line-integrated emission intensities at the center (distance = 0),

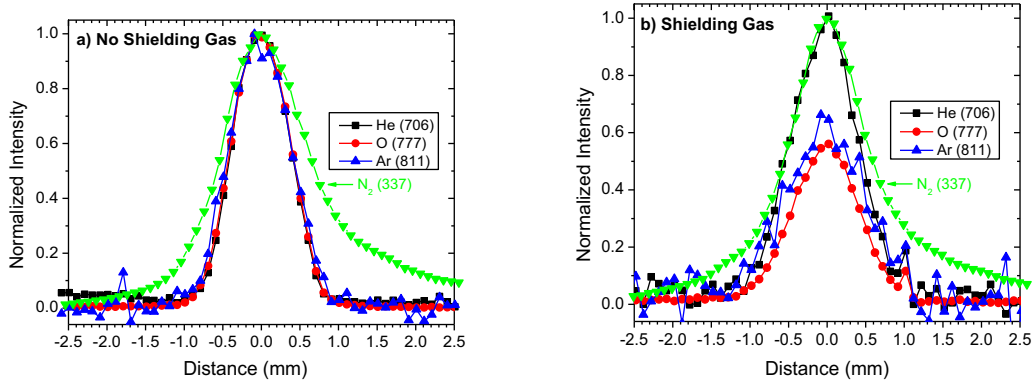


**Figure 3.** Horizontal line-integrated emission intensities from He, O, Ar and N<sub>2</sub> recorded by scanning the optical axis along the plane perpendicular to the plasma jet axis (figure 2). The  $x$ -axis distance,  $d$ , is that between the optical axis and plasma jet axis. He flow rate = 2.0 slm. He emission intensities were normalized to unity at the center ( $d = 0$ ). (a) No N<sub>2</sub> shielding gas flow. O, Ar and N<sub>2</sub> emission intensities were also normalized to unity at the center. (b) N<sub>2</sub> shielding gas flow rate = 4.5 slm. O, Ar and N<sub>2</sub> emission intensities were normalized with the same O-to-He, Ar-to-He and N<sub>2</sub>-to-He emission normalization ratios as were used in (a) to reveal any changes in relative O, Ar and N<sub>2</sub> emission intensities relative to He emission, caused by the presence of the shielding gas.

with no shielding gas (figure 3(a)) are normalized to unity. The emission profiles of He, Ar and O are similar; N<sub>2</sub> emission extends farther from the plasma jet axis. With N<sub>2</sub> shielding gas flowing (figure 3(b)) He emission intensity was again normalized to unity at the center. Using the same normalization factors, relative to He, that were used in figure 3(a), emission from O and Ar were found to drop by nearly half in the center, while N<sub>2</sub> emission was the same intensity and shape as in figure 3(a). This is at least qualitatively as expected. The shielding gas suppresses air from diffusing into the center of the plasma jet, while the substitution of static air with flowing N<sub>2</sub> caused little change in the amount of N<sub>2</sub> in the plasma jet.

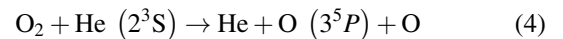
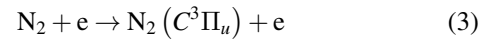
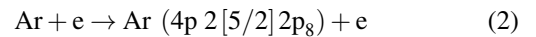
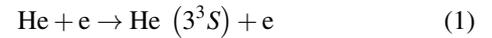
In some cases, the emission profiles were moderately asymmetric with respect to distance from the center. This is most prevalent for N<sub>2</sub> (e.g. figure 3(a)), due to the fact that the emission is the most intense and N<sub>2</sub> number density maximizes with increasing radial distance. This asymmetry is due to random small movements of the jet above or below the tube axis. (Note that the measurements are not significantly affected by displacements in the horizontal direction.) Since the Abel inversions assumed azimuthal symmetry, we took the average of the intensity at distance  $+d$  and  $-d$  from the center to be the intensity at  $+d$  and at  $-d$ .

### 3.2. Theory of self-actinometry

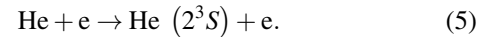
Raw emission intensity measurements such as those in figure 3 are only qualitatively related to species number densities. Often emission intensities for species of interest are divided by emission intensities from rare gases present at known concentrations to derive qualitative relative and even absolute number densities. This actinometry method has been successfully used for selected species in low pressure plasmas. Necessary but not sufficient requirements for actinometry are that emission be excited by electron impact from the ground state, that the electron impact excitation cross section of the emitter match the relative energy dependence of the rare gas (usually Ar 2p<sub>1</sub> emission at 750.4 nm is best for this purpose),

that emission is not a result of dissociative excitation, and that quenching of excited states by collisions with gas molecules is slow compared with radiative decay, or that the quenching rate is accurately known.

While emissions from He, Ar and N<sub>2</sub> are excited by electron impact, excited O-atoms are produced mainly by Penning dissociative excitation of O<sub>2</sub> in collisions with He metastables (He\*) [35–37]. The excitation reactions are,



where the He (2<sup>3</sup>S) metastable state was created by electron impact,



Stepwise excitation the He(3<sup>3</sup>S) emitting state via electron impact from the 2<sup>3</sup>S metastable state can be ignored (<4% from an unpublished modeling calculation), since the metastable state number density is quite low at atmospheric pressure in air.

Since Ar is one of the species that we wish to detect, Ar cannot be used as the actinometer gas (the density of the actinometer gas must be known). In addition, O emission results from He metastable dissociative excitation of O<sub>2</sub> and quenching of excited states cannot be ignored (discussed below) at atmospheric pressure. Consequently, standard actinometry cannot be used to obtain even semi-qualitative relative number densities for this atmospheric pressure plasma.

Species absolute number densities were instead determined by a form of actinometry in which a known small amount of

gas added to the main He flow produces a small but measurable change in the emission intensity characteristic of that species. This ‘self-actinometry’ method allows an absolute calibration of emission intensities to produce absolute number densities, most easily expressed as mole fractions. We stress that this is not classical actinometry. In classical actinometry, one would for example measure the N<sub>2</sub>-to-He or Ar-to-He ratio as a function of a condition such as axial position and simply take the ratio as an indication of relative number density for those conditions. Because the gas composition changes with condition, the ionization pathways and loss processes are altered, possibly resulting in a substantial change in the electron energy distribution function (EEDF) that will influence the relative actinometry proportionality constant. This could easily result in orders of magnitude errors in relative N<sub>2</sub> or Ar mole fraction determined by actinometry. Furthermore, it would be difficult to compute or measure the actinometric constant to obtain absolute mole fractions because the EEDF is not known.

In self-actinometry, that we have reported for low pressure plasmas, and here are extending to atmospheric pressure, we are introducing a small amount of the species of interest (i.e. N<sub>2</sub>, O<sub>2</sub>, or Ar) to a plasma that already contains generally much higher levels of these species. The perturbation to the plasma is therefore relatively small, as sensed by the small change in He emission and He-to-Ar ratio for added O<sub>2</sub>. The calibration is done for each position, thereby eliminating the problems

caused by large changes in plasma conditions as a function of position. If one were to study dependencies on other conditions, such as flow rate or power, one would similarly do a calibration of the emission intensity for each flow rate or power, and not simply assume that the emission ratio scales with species number density with a flow rate-independent, or power-independent proportionality constant.

In the absence of trace additions of Ar, O<sub>2</sub> or N<sub>2</sub> to the He feed gas, and ignoring any species produced by the plasma, the total number density,  $n_T$ , at a particular radial and axial location ( $r, z$ ) in the plasma jet, is given by the sum of the component number densities,

$$n_T = n_{He} + n_{Ar} + n_{O_2} + n_{N_2}. \quad (6)$$

Taking Ar as an example, the intensity of Ar emission at 811 nm is given by

$$I_{Ar}^0 = a_{Ar}^0 n_e^0 n_{Ar} Y_{Ar}^0 \quad (7)$$

where  $a_{Ar}^0$  is a proportionality constant that depends on the electron energy distribution,  $n_e^0$  is the electron density, the superscript 0 refers to the condition in the absence of trace gas addition to the He flow, and  $Y_{Ar}^0$  is the yield for emission of a photon by the excited state after it is formed by electron impact.  $Y_{Ar}^0$  is given by

$$Y_{Ar}^0 = \frac{b_{Ar} A_{Ar}}{A_{Ar} + k_{q,Ar}^{He} n_{He} + k_{q,Ar}^{Ar} n_{Ar} + k_{q,Ar}^{O_2} n_{O_2} + k_{q,Ar}^{N_2} n_{N_2} + k_{q,Ar}^e n_e^0} \quad (8)$$

where  $b_{Ar}$  is the branching ratio for the transition in Ar,  $A_{Ar}$  is the Einstein A coefficient for the transition, and the quenching rate constants  $k_q$  correspond to the superscripted species.

If a trace of Ar at a flow rate  $f_{Ar}$  is added to the He feed gas flow  $f_{He}$ , producing an additional  $\Delta n_{Ar}$  in the plasma at

( $r, z$ ), a change (usually, but not necessarily an increase) in Ar emission results in a new intensity  $I_{Ar}$ , given by

$$I_{Ar} = a_{Ar} n_e (n_{Ar} + \Delta n_{Ar}) Y_{Ar} \quad (9)$$

with  $Y_{Ar}$  now given by

$$Y_{Ar} = \frac{b_{Ar} A_{Ar}}{A_{Ar} + k_{q,Ar}^{He} n_{He} + k_{q,Ar}^{Ar} [n_{Ar} + \Delta n_{Ar}] + k_{q,Ar}^{O_2} n_{O_2} + k_{q,Ar}^{N_2} n_{N_2} + k_{q,Ar}^e n_e}. \quad (10)$$

Similarly, the intensity and yield for He in the absence of added Ar are given by

$$I_{He}^0 = a_{He}^0 n_e^0 n_{He} Y_{He}^0. \quad (11)$$

$$Y_{He}^0 = \frac{b_{He} A_{He}}{A_{He} + k_{q,He}^{He} n_{He} + k_{q,He}^{Ar} n_{Ar} + k_{q,He}^{O_2} n_{O_2} + k_{q,He}^{N_2} n_{N_2} + k_{q,He}^e n_e^0} \quad (12)$$

while in the presence of trace added Ar, they are

$$I_{\text{He}} = a_{\text{He}} n_e n_{\text{He}} Y_{\text{He}} \quad (13)$$

$$Y_{\text{He}} = \frac{b_{\text{He}} A_{\text{He}}}{A_{\text{He}} + k_{q,\text{He}}^{\text{He}} n_{\text{He}} + k_{q,\text{He}}^{\text{Ar}} [n_{\text{Ar}} + \Delta n_{\text{Ar}}] + k_{q,\text{He}}^{\text{O}_2} n_{\text{O}_2} + k_{q,\text{He}}^{\text{N}_2} n_{\text{N}_2} + k_{q,\text{He}}^e n_e}. \quad (14)$$

As shown in figure 4, the addition of trace Ar to the He flow causes small changes in He emission, likely due to small changes in the electron density and/or energy distribution. If the perturbations affect the Ar excitation the same way they affect He, then  $a_{\text{Ar}} n_e$  can be determined from

$$\frac{a_{\text{He}} n_e}{a_{\text{He}}^0 n_e^0} = \frac{I_{\text{He}} Y_{\text{He}}^0}{I_{\text{He}}^0 Y_{\text{He}}} = \frac{a_{\text{Ar}} n_e}{a_{\text{Ar}}^0 n_e^0}. \quad (15)$$

Equating of the third term in equation (15) with the first two terms would be a trivial assumption if solely  $n_e$  were affected by trace Ar addition. It was not possible to experimentally determine if changes in the electron energy distribution would make this an invalid assumption for trace Ar addition to He, but it is shown below (in the section on calibrations) that addition of trace O<sub>2</sub> made negligible changes in the He/Ar emission intensity ratio (Ar from air diffusion into the He feed gas) at all three axial positions.

Dividing equation (9) by equation (7), rearranging, and substituting  $\frac{I_{\text{He}} Y_{\text{He}}^0}{I_{\text{He}}^0 Y_{\text{He}}}$  from equation (15) for  $\frac{a_{\text{Ar}} n_e}{a_{\text{Ar}}^0 n_e^0}$  yields the expression for  $n_{\text{Ar}}$

$$n_{\text{Ar}} = \frac{\Delta n_{\text{Ar}}}{\left(\frac{I_{\text{He}}^0 Y_{\text{He}}}{I_{\text{He}} Y_{\text{He}}^0}\right) \left(\frac{I_{\text{Ar}} Y_{\text{Ar}}^0}{I_{\text{Ar}}^0 Y_{\text{Ar}}}\right) - 1}. \quad (16)$$

The plasma extinguishes before the impurities in He from both the added trace gas and inward diffusing air become substantial (impurities lower the population of high energy electrons, leading to a reduction of the ionization rate for a given electric field, a resulting drop in electric field near the tip and radial edge of the jet, and an extinguishing of the plasma). Hence,  $\Delta n_{\text{Ar}}$  is given to a good approximation by

$$\Delta n_{\text{Ar}} = \frac{f_{\text{Ar}}}{f_{\text{He}}} n_{\text{T}}. \quad (17)$$

Finally, combining equations (16) and (17), the mole fraction of Ar in the plasma is,

$$\frac{n_{\text{Ar}}}{n_{\text{T}}} = \frac{\frac{f_{\text{Ar}}}{f_{\text{He}}}}{\left(\frac{I_{\text{He}}^0 Y_{\text{He}}}{I_{\text{He}} Y_{\text{He}}^0}\right) \left(\frac{I_{\text{Ar}} Y_{\text{Ar}}^0}{I_{\text{Ar}}^0 Y_{\text{Ar}}}\right) - 1} \quad (18)$$

where the quantities on the right hand side of equation (18) are measured (intensities), known (flows), or can be calculated (yields).

Similar to trace Ar addition, small changes in He emission are produced by trace addition of N<sub>2</sub> or O<sub>2</sub>. (Model predictions of the small effect of minute additions of N<sub>2</sub> on He emission compare favorably with experiments, as presented in the

appendix). An analogous equation holds for the number density of N<sub>2</sub>, determined from N<sub>2</sub> C → B emission, with all the Ar subscripted variables in equation (18) replaced by the corresponding values for N<sub>2</sub>:

$$\frac{n_{\text{N}_2}}{n_{\text{T}}} = \frac{\frac{f_{\text{N}_2}}{f_{\text{He}}}}{\left(\frac{I_{\text{N}_2}^0 Y_{\text{N}_2}}{I_{\text{N}_2} Y_{\text{N}_2}^0}\right) \left(\frac{I_{\text{N}_2} Y_{\text{N}_2}^0}{I_{\text{N}_2}^0 Y_{\text{N}_2}}\right) - 1}. \quad (19)$$

The O-atom 777 nm emission intensities  $I_{\text{O}}$  and  $I_{\text{O}}^0$  with and without added O<sub>2</sub> are given, respectively, by

$$I_{\text{O}} = a_{\text{O}} n_{\text{He}^*} (n_{\text{O}_2} + \Delta n_{\text{O}_2}) Y_{\text{O}} \quad (20)$$

$$I_{\text{O}}^0 = a_{\text{O}}^0 n_{\text{He}^*}^0 n_{\text{O}_2} Y_{\text{O}}^0 \quad (21)$$

where  $a_{\text{O}}$  is the rate constant for production of the excited state O\* from collisions of O<sub>2</sub> with He\*, (see equation 4) which does not depend on electron temperature, hence  $a_{\text{O}}^0 = a_{\text{O}}$ . Here, He\* is the He(2<sup>3</sup>S) metastable state. Following the same procedure as with electron impact excitation of Ar,

$$n_{\text{O}_2} = \frac{\Delta n_{\text{O}_2}}{\left(\frac{n_{\text{He}^*}^0}{n_{\text{He}^*}}\right) \left(\frac{I_{\text{O}} Y_{\text{O}}^0}{I_{\text{O}}^0 Y_{\text{O}}}\right) - 1}. \quad (22)$$

Equation (22) indicates that in order to determine the absolute number density of O<sub>2</sub> from O-atom 777 nm emission, an analysis of He\* production and loss is required to find the density of metastables. At steady-state,  $\frac{dn_{\text{He}^*}}{dt} = 0$ , and the mass balance with added O<sub>2</sub> is given by:

$$k_{\text{He}^*} n_{\text{He}} n_e = n_{\text{He}^*} (k_{\text{He}^*}^{\text{He}} n_{\text{He}} + k_{\text{He}^*}^{\text{Ar}} n_{\text{Ar}} + k_{\text{He}^*}^{\text{O}_2} [n_{\text{O}_2} + \Delta n_{\text{O}_2}] + k_{\text{He}^*}^{\text{N}_2} n_{\text{N}_2} + k_{\text{He}^*}^e n_e + F) \quad (23)$$

where  $k_{\text{He}^*}$  is rate constant for formation of He\* by collisions of electrons with He. Rate constants  $k_{\text{He}^*}^{\text{He}}$ ,  $k_{\text{He}^*}^{\text{Ar}}$ ,  $k_{\text{He}^*}^{\text{O}_2}$ ,  $k_{\text{He}^*}^{\text{N}_2}$  and  $k_{\text{He}^*}^e$  represent loss of He\* through collisions with the super-scripted species, and  $F$  is the volumetric loss rate of He\* out of the observation region through convective transport. It turns out that loss of species through transport is slow compared to the reactions forming and destroying He\* and can be ignored (i.e.  $F = 0$ ). Loss of He\* through collisions with He\* and He<sub>2</sub>\* can also be ignored as a loss of He\*. Without added O<sub>2</sub>

$$k_{\text{He}^*}^0 n_{\text{He}} n_e^0 = n_{\text{He}^*}^0 (k_{\text{He}^*}^{\text{He}} n_{\text{He}} + k_{\text{He}^*}^{\text{Ar}} n_{\text{Ar}} + k_{\text{He}^*}^{\text{O}_2} n_{\text{O}_2} + k_{\text{He}^*}^{\text{N}_2} n_{\text{N}_2} + k_{\text{He}^*}^e n_e^0). \quad (24)$$

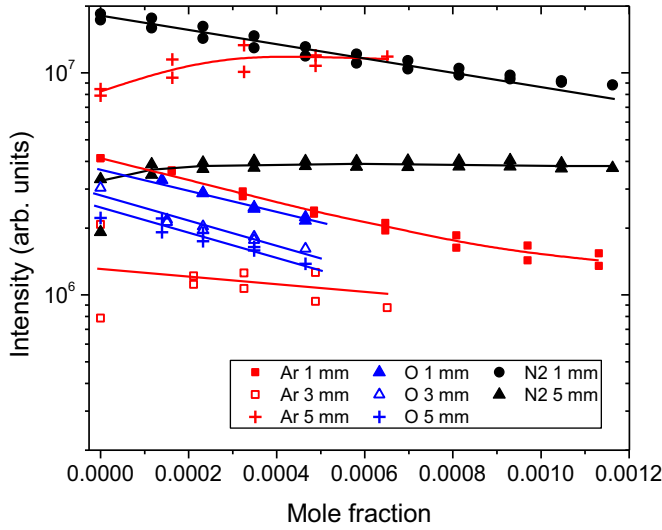


**Figure 4.** On-axis He emission intensity (706 nm) at 1 mm, 3 mm and 5 mm axial distance from the nozzle, as a function of N<sub>2</sub>, O<sub>2</sub>, and Ar addition to the feed gas to achieve the indicated mole fraction.

The small dependence of  $k_{\text{He}^*}^c$  on a small change in  $T_e$  is ignored (hence no superscript 0 is used). Letting  $k_{\text{He}^*}^{\text{He}} n_{\text{He}} + k_{\text{He}^*}^{\text{Ar}} n_{\text{Ar}} + k_{\text{He}^*}^{\text{O}_2} n_{\text{O}_2} + k_{\text{He}^*}^{\text{N}_2} n_{\text{N}_2} = Q$ , and dividing equation (24) by equation (23) yields,

$$\frac{n_{\text{He}^*}^0}{n_{\text{He}^*}} = \frac{k_{\text{He}^*}^0 n_e^0 Q + k_{\text{He}^*}^{\text{O}_2} \Delta n_{\text{O}_2} + k_{\text{He}^*}^c n_e}{k_{\text{He}^*} n_e Q + k_{\text{He}^*}^c n_e^0}. \quad (25)$$

The energy dependences of the cross sections for electron impact excitation of He to its metastable states are similar to that for the 3s<sup>3</sup>S state that is emitting at 706 nm. Specifically, the cross section for electron impact excitation of the metastable state is a nearly constant 2.0–2.5 × 10<sup>−18</sup> cm<sup>2</sup> from threshold (20.6 eV) to 40 eV, and excitation of the state responsible for the 706 nm emission by electron impact is likewise a nearly constant 3–4 × 10<sup>−19</sup> cm<sup>2</sup> from just above threshold (22.6 eV) to 40 eV [38]. If the addition of trace gas in the calibration process were to change  $T_e$  for example from 2.4 to 2.6 eV, the rate constant for 1<sup>1</sup>S → 2<sup>1</sup>S would increase by a factor of 1.9 while that for 1<sup>1</sup>S → 3<sup>1</sup>S would increase 2.0-fold. Nothing close to a two-fold change in He emission was observed. Consequently, any smaller change in plasma conditions affects He emission excitation and He metastable formation in the same way, and one can assume that  $\frac{k_{\text{He}^*}^0 n_e^0}{k_{\text{He}^*} n_e} \approx \frac{a_{\text{He}^*}^0 n_e^0}{a_{\text{He}^*} n_e} = \frac{I_{\text{He}}^0 Y_{\text{He}}}{I_{\text{He}} Y_{\text{He}}^0}$ , hence equation (22) yields,

$$n_{\text{O}_2} = \frac{\Delta n_{\text{O}_2}}{\left( \frac{I_{\text{He}}^0 Y_{\text{He}}}{I_{\text{He}} Y_{\text{He}}^0} \right) \left( \frac{Q + k_{\text{He}^*}^{\text{O}_2} \Delta n_{\text{O}_2} + k_{\text{He}^*}^c n_e}{Q + k_{\text{He}^*}^c n_e^0} \right) \left( \frac{I_{\text{O}_2} Y_{\text{O}_2}^0}{I_{\text{O}_2}^0 Y_{\text{O}_2}} \right) - 1}. \quad (26)$$

Radiative rates and quenching rate constants are summarized in table 1 (bold numbers are estimates). Previous measurements indicated that the average gas temperature in the plasma is 900 K, thus the quenching rate constants were selected at 900 K, if available. Otherwise they were estimated using

$\frac{k(T_2)}{k(T_1)} = \left( \frac{T_2}{T_1} \right)^{0.5}$ . The maximum quenching rates at maximum species number densities (5 mm from nozzle) are presented in table 2. Table 3 shows the effect of trace gas addition on emission yields and on quenching of He\*. The quenching factor  $F_Q$  is defined as the mole fraction determined with quenching accounted for, divided by the mole fraction determined without accounting for quenching (i.e. setting all quenching rate constants equal to zero),

$$\frac{n_{\text{Ar, N}_2 \text{ or O}_2}(\text{with quenching})}{n_{\text{Ar, N}_2 \text{ or O}_2}(\text{without quenching})} = F_Q. \quad (27)$$

In all cases, quenching by electrons can be ignored. For Ar actinometry, the small amount of added Ar causes a negligible increase in the total quenching of Ar (2p<sub>8</sub>) and He (3s<sup>3</sup>S) at 3 mm and 5 mm from the nozzle, hence  $\frac{Y_{\text{He}}^0}{Y_{\text{He}}} \approx \frac{Y_{\text{Ar}}^0}{Y_{\text{Ar}}} = 1$  in equation (18). However, at 1 mm, where neither O<sub>2</sub> nor N<sub>2</sub> are present for quenching of He (3s<sup>3</sup>S), the contribution by trace Ar addition becomes significant and must be accounted for.

For N<sub>2</sub>, loss of N<sub>2</sub> (C<sup>3</sup>Π<sub>u</sub>) is mainly by emission and quenching by He and O<sub>2</sub>, with negligible N<sub>2</sub> quenching. Thus, addition of N<sub>2</sub> would not affect N<sub>2</sub> (C<sup>3</sup>Π<sub>u</sub>) emission yield  $\left( \frac{Y_{\text{N}_2}^0}{Y_{\text{N}_2}} = 1 \right)$ . Loss of He (3s<sup>3</sup>S) is dominated by N<sub>2</sub> quenching, however, and at 1 mm from the nozzle, where insignificant amounts of ambient N<sub>2</sub> have diffused into the plasma, the small addition of N<sub>2</sub> leads to significant changes in the emission yield of He  $\left( \frac{Y_{\text{He}}^0}{Y_{\text{He}}} = 1.44 \right)$ , making the inclusion of quenching important with  $F_Q = 1.44$ . At 5 mm from nozzle, a large amount of N<sub>2</sub> is present in the plasma, thus the addition of trace N<sub>2</sub> is not as impactful  $\left( \frac{Y_{\text{He}}^0}{Y_{\text{He}}} = 1.04 \right)$ . However, due to the closeness of  $\frac{I_{\text{N}_2}^0}{I_{\text{He}}^0}$  (no N<sub>2</sub> addition) and  $\frac{I_{\text{N}_2}}{I_{\text{He}}}$  (with N<sub>2</sub> addition) (figure 4), the quenching factor remains important ( $F_Q = 1.83$ ).

Finally, addition of a small amount of O<sub>2</sub> to the feed gas will cause a negligible increase of the loss rate of O (3p<sup>5</sup>P)  $\left( \frac{Y_{\text{O}_2}^0}{Y_{\text{O}_2}} \approx 1 \right)$ . Similar to N<sub>2</sub>, little air diffuses into the plasma at 1 mm, hence trace addition of O<sub>2</sub> severely impacts both the He emission yield  $\left( \frac{Y_{\text{He}}^0}{Y_{\text{He}}} = 1.44 \right)$  and the He\* quenching rate  $\left( \frac{Q}{Q + k_{\text{He}^*}^{\text{O}_2} \Delta n_{\text{O}_2}} = 0.029 \right)$ , leading to very large quenching effect ( $F_Q = 0.0257$ ). This effect is greatly reduced at 3 and 5 mm from nozzle, and the quenching factor becomes  $F_Q \approx 0.85$ .

Under the assumption that the excitation rate constants of Ar, N<sub>2</sub>, He and He\*, the various emission yields, and the excitation and quenching rates of He\* each behave similarly as electron number density, electron temperature and mole fractions change from plasma center to the edge with or without shielding gas. i.e.  $\left( \frac{a_{\text{He}}^0(r=0)}{a_{\text{He}}^0(r)} = \frac{a_s^0(r=0)}{a_s^0(r)}, \frac{Y_{\text{He}}^0(r=0)}{Y_{\text{He}}^0(r)} = \frac{Y_s^0(r=0)}{Y_s^0(r)}, \frac{Q(r)}{Q} = \frac{k_{\text{He}^*}^0(r)}{k_{\text{He}^*}^0} \right)$ , where  $S$  can be Ar, N<sub>2</sub>, or O<sub>2</sub>. Under these conditions, the radial emission intensity,  $I_r^s/I_{r_e}^s$ , can be converted into radial mole fractions,  $\frac{n_s^0(r)}{n_T}$ , as follows

**Table 1.** Einstein A-coefficients ( $10^6 \text{ s}^{-1}$ ) and quenching rate constants ( $10^{-10} \text{ cm}^3 \text{ s}^{-1}$ ) for the states indicated in the first column at 900 K. (a) An upper limit, assumed to be the same as quenching by  $\text{N}_2$ . (b) O (777) ( $3p^5P$ ) quenching rate constants assumed to be the same as O (844) ( $3p^3P$ ). Bold numbers are estimated quenching rate constants.

State	A	Quenching rate constants				
		He	Ar	$\text{O}_2$	$\text{N}_2$	e
Ar (811) ( $4p\ 2[5/2]\ 2p_8$ )	36.6 [39]	0.24 [40]	0.42 [40]	11 [40]	6.1 [40]	—
He (706.5) ( $3s^3S$ )	27.9 [41]	0 [42]	< <b>12</b> <sup>(a)</sup>	< <b>12</b> <sup>(a)</sup>	12 [43]	—
O (777) ( $3p^5P$ )	36.9 -44]	0.12 [45]	<b>0.36</b> <sup>(b)</sup>	18 [46]	<b>7.4</b> <sup>(b)</sup>	—
O (844) ( $3p^3P$ )	32.2 [44]	0.26 [47]	0.36 [47]	11 [47]	7.4 [47]	—
$\text{N}_2$ ( $\text{C}^3\Pi_u$ )	28.6 [48]	0.017[49]	0.0097 [50]	5.0 [51]	0.23 [51]	1000 [52]
He ( $2s^3S$ )	—	< $10^{-5}$ [53]	3.0 [54]	6.0 [54]	3.0 [54, 55]	6.5 [56]

**Table 2.** Maximum quenching rates ( $10^6 \text{ s}^{-1}$ ) for the states indicated in the first column at maximum number densities ( $\text{cm}^{-3}$ ) given along the second row. Bold numbers are estimated quenching rates, corresponding to the bold numbers in table 1.

State	A	Maximum quenching rates ( $10^6 \text{ s}^{-1}$ )				
		He $2 \times 10^{19}$	Ar $4 \times 10^{15}$	$\text{O}_2\ 5 \times 10^{16}$	$\text{N}_2\ 2 \times 10^{17}$	e $1 \times 10^{13}$
Ar (811) ( $4p\ 2[5/2]\ 2p_8$ )	36.6	490	0.17	55	120	—
He (706.5) ( $3s^3S$ )	27.9	0	< <b>5</b>	< <b>60</b>	250	—
O (777) ( $3p^5P$ )	36.9	240	<b>0.15</b>	91	<b>150</b>	—
O (844) ( $3p^3P$ )	32.2	520	0.15	55	150	—
$\text{N}_2$ (337) ( $\text{C}^3\Pi_u$ )	28.6	35	0.0039	25	4.6	1.0
He ( $2s^3S$ )	—	<0.02	1.2	30	60	0.0065

**Table 3.** Effect of trace gas (Ar,  $\text{N}_2$  or  $\text{O}_2$ ) addition on emission yields ( $\frac{Y^0}{Y}$ ), He\* quenching rates,  $\frac{Q}{Q+k_{\text{He}^*}^{\text{O}_2} \Delta n_{\text{O}_2}}$ , see equation (25), and the resulting quenching factors  $F_Q$  (equation (27)).

Distance from nozzle	Ar			$\text{N}_2$		
	$\frac{Y_{\text{He}}^0}{Y_{\text{He}}}$	$\frac{Y_{\text{Ar}}^0}{Y_{\text{Ar}}}$	$F_Q$	$\frac{Y_{\text{He}}^0}{Y_{\text{He}}}$	$\frac{Y_{\text{N}_2}^0}{Y_{\text{N}_2}}$	$F_Q$
1 mm	1.44	1.01	1.41	1.44	1.00	1.44
3 mm	1.05	1.00	1.06	—	—	—
5 mm	1.04	1.00	1.05	1.04	1.00	1.83
Distance from nozzle	$\text{O}_2$					
	$\frac{Y_{\text{He}}^0}{Y_{\text{He}}}$	$\frac{Y_{\text{O}_2}^0}{Y_{\text{O}_2}}$	$\frac{Q}{Q+k_{\text{He}^*}^{\text{O}_2} \Delta n_{\text{O}_2}}$	$F_Q$	—	—
1 mm	1.44	1.07	0.029	0.0257	—	—
3 mm	1.05	1.05	0.907	0.854	—	—
5 mm	1.04	1.04	0.921	0.841	—	—

$$\frac{n_S^r(r)}{n_T} = \frac{I_S/I_{\text{He}}(r)}{I_S^0/I_{\text{He}}^0} \frac{n_S}{n_T}. \quad (28)$$

### 3.3. Self-actinometry calibration

Calibrations were carried out for  $\text{N}_2$ ,  $\text{O}_2$ , and Ar at 1 mm, 3 mm and 5 mm distances from the nozzle (calibration of  $\text{N}_2$  at 3 mm was assumed to be an average of the nearly identical 1 mm and 5 mm values). In the calibrations process, line-integrated emission intensities across the axial center of the plasma were recorded as a function of the addition of trace amounts of  $\text{N}_2$ ,  $\text{O}_2$ , or Ar to the He feed gas. The intensities of Ar, O and  $\text{N}_2$ , ratioed to He emission, were recorded as a function of mole fraction of added Ar,  $\text{O}_2$  and  $\text{N}_2$ , as shown in figure 5. The

slopes of the linear least squares fits provided the calibration. This calibration was then applied to the radial distribution of species emissions (derived by Abel inverting line-integrated lateral emission profiles) to produce the final radial distribution of species mole fractions. Since the calibrations were carried out at the three axial positions by probing along the most intense line-integrated radial emissions passing through the plasma jet axis, there is a bit of a mismatch between the calibration and the radially-resolved, Abel-inverted emissions. This is less of an issue at 3 and 5 mm from the nozzle, where significant air diffusion has occurred such that the radial distribution of air species is relatively flat, but may lead to increased error in the absolute calibration of species mole fractions far from the axis at 1 mm from the nozzle, where concentration gradients are large.

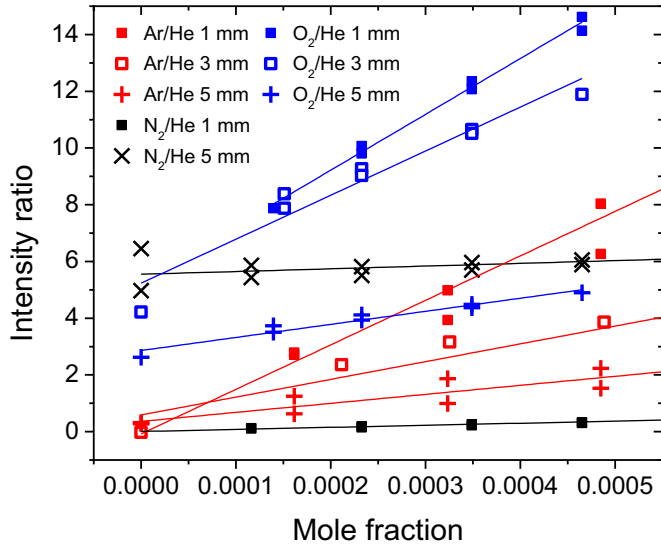


**Figure 5.** N<sub>2</sub>/He, O<sub>2</sub>/He, and Ar/He intensity ratios at 1 mm, 3 mm and 5 mm axial distance from the nozzle as a function of N<sub>2</sub>, O<sub>2</sub>, and Ar addition to the feed gas to achieve the indicated mole fraction. The lines are least-square linear fits. The calibrations, determined from the slopes of the fits, were ( $\times 10^3$ ) 15.7, 6.2 and 3.2 for Ar, and 19.7, 15.5 and 4.6 for O<sub>2</sub> at 1, 3 and 5 mm, respectively. The slopes ( $\times 10^3$ ) for N<sub>2</sub> were 0.73 and 0.96 at 1 and 5 mm.

The He 706 nm emission may be a relatively good indicator of changes in the relative population of electrons in the >20 eV region that are also important for creating He metastables. The He 706 nm emission may not be very representative of the lower energy electrons that are effective in exciting N<sub>2</sub>(C<sup>3</sup>Π<sub>u</sub>) and Ar emission, however. Some insight into this may be obtained by noting the effect of adding small amounts of O<sub>2</sub> to the He feed. Since the He/Ar number density ratio remains constant, the He/Ar intensity can be used to estimate  $\frac{a_{He}}{a_{Ar}}$  as a function of  $\Delta n_{O_2}$  from the relationship,

$$\frac{a_{He}}{a_{Ar}} = \left( \frac{n_{Ar}}{n_{He}} \right) \frac{I_{He}}{I_{Ar}} \frac{Y_{Ar}}{Y_{He}}. \quad (29)$$

As shown in figure 6,  $\frac{I_{He}}{I_{Ar}}$  (with or without multiplying by the factor  $\frac{Y_{Ar}}{Y_{He}}$  that corrects for small changes in quenching rates) remains nearly constant as a function of added O<sub>2</sub> at 3 and 5 mm, and drop only modestly at 1 mm, indicating little change in the distributions of electron energies with this small amount of impurity, and justifying the use of He 706 nm emission in this actinometry role.

### 3.4. Radial mole fraction of air impurity diffusing into the plasma jet

Emission intensities of N<sub>2</sub>, O<sub>2</sub>, and Ar were measured as a function of radial distance, at different axial positions away from the nozzle. The intensity was then converted into mole fractions as described above (presented in figure 7). Corrections based on quenching of excited states were applied. The error bars were calculated from standard propagation-of-error analysis and are based on the following errors: 1% in gas flow

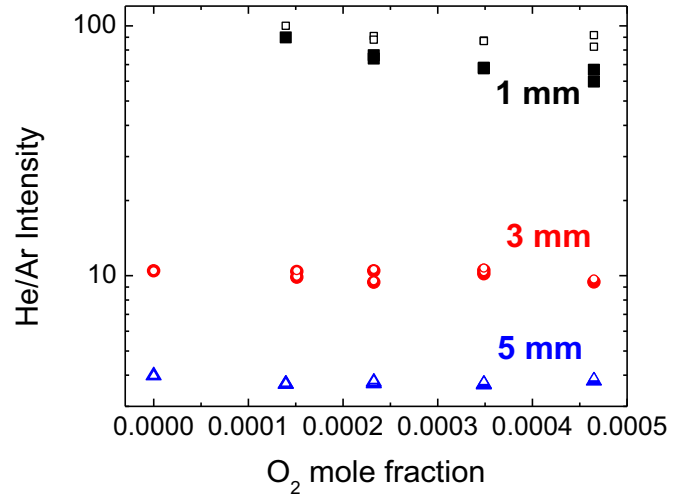


**Figure 6.** Line-integrated radial  $\frac{I_{He}}{I_{Ar}}$  as a function of added O<sub>2</sub> mole fraction (solid symbols) and  $\frac{I_{He}}{I_{Ar}}$  (open symbols, with quenching effect accounted for) at 1 mm, 3 mm, and 5 mm axial distance from the nozzle.

rate, 10%–30% in quenching rate constants, as reported in the literature (50% error for estimated rate constants), and errors in determination of slopes and intercepts of intensity ratio vs added trace gas mole fraction (figure 5).

The uncertainty in the derived number densities vary substantially, depending on species and conditions. For example, the uncertainty in N<sub>2</sub> concentration at 3 and 5 mm axial distance in figure 7 is rather large ( $\sim \pm 50\%$ ), despite the fact that the emission signals are intense, while the uncertainty is only a few % in Ar concentration at these locations, despite the fact that Ar is present at much lower concentration and is weakly emitting. It is also hard to compare errors in this method with traditional actinometry, where unknown errors such as dissociative excitation, processes other than electron impact leading to production of emission, radiation trapping, etc make it highly suspect as even a qualitative method. The self-actinometry method we describe here ‘cancels-out’ such problems.

Figure 7 shows that the measured mole fraction profiles of N<sub>2</sub>, O<sub>2</sub> and Ar at 3 mm and 5 mm from the nozzle are fairly flat across the 1.0 mm diameter of the plasma jet, with N<sub>2</sub>:O<sub>2</sub>:Ar percentages of  $90.0 \pm 3.3$ : $7.4 \pm 3.0$ : $0.6 \pm 0.3$  at 5 mm and  $80.6 \pm 7.4$ : $17.7 \pm 6.8$ : $1.7 \pm 0.8$  at 3 mm. Given the complexities in the optical emission excitation processes (particularly O-atom emission), as well as the added uncertainties introduced by the Abel inversion, the agreement of the measured number densities with the composition of air (78:21:1) is quite remarkable, especially at 5 mm.

At 1 mm distance from the nozzle, both O<sub>2</sub> and Ar are present at the center of the plasma, while N<sub>2</sub> is absent (exceedingly low mole fraction). This is due to trace O<sub>2</sub> (or possibly H<sub>2</sub>O) and Ar impurities in the He feed gas. The ambient N<sub>2</sub> (i.e. air) diffusion front is  $\sim 2$  mm radial distance from the jet axis at 1 mm axial distant from the nozzle. With 4.5 slm N<sub>2</sub> shielding gas, O<sub>2</sub> and Ar mole fractions do not change at 1 mm since their values still come from the He gas feed impurities.

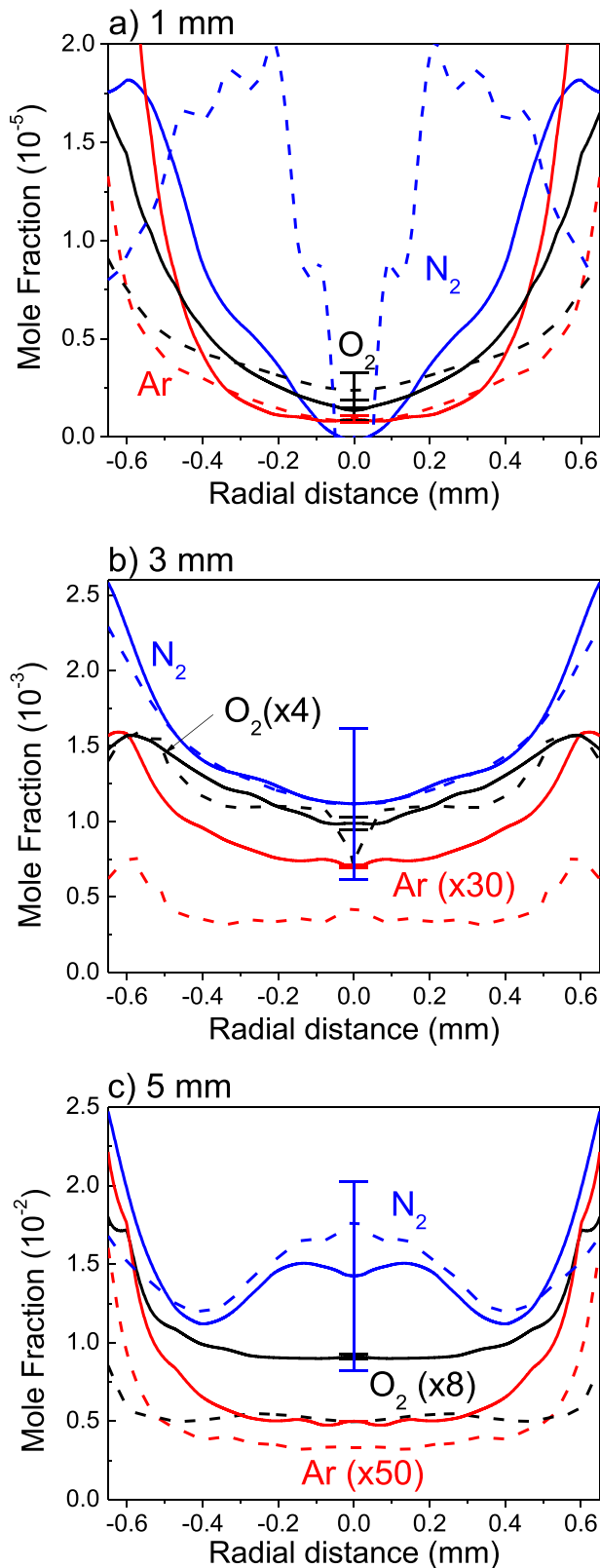


**Figure 7.** Experimental radial profiles of air species mole fraction, with (dashed lines) and without (solid lines) shielding gas, at 1 mm, 3 mm, and 5 mm axial distance from the nozzle. The error bars were computed from standard propagation-of-error analysis.

At 5 mm, however, the shielding gas flow reduces  $O_2$  and  $Ar$  content in the plasma jet by a factor of 2–4.  $N_2$  content at the center increases by a factor of 1.24, close to the expected 1.28 increase in  $N_2$  content between the pure  $N_2$  shielding gas and air. Furthermore, as expected, the  $O_2$  and  $Ar$  mole fractions decrease and the nitrogen mole fraction increases in the presence of shielding gas (figure 7).

### 3.5. Comparison with simulations

A two-dimensional numerical simulation of a non-equilibrium APPJ in helium, with co-axial nitrogen shielding gas was also performed. The shielding gas provided a curtain hindering penetration of the ambient gas (here dry air 78% $N_2$ –21% $O_2$ –1% $Ar$ ) into the helium jet. Details of the model are given elsewhere [57]. Briefly, a neutral gas convective mass and heat transport model was combined with a fluid plasma dynamics model to predict the APPJ discharge characteristics. The model predicted (among other quantities) the 2D profiles of gas temperature and species concentration, along with electron density and temperature, with and without shielding gas. Simulation predictions of ambient species mole fractions in the plasma jet, were compared to experimental measurements. Results for an APPJ with nitrogen shielding gas were compared to an otherwise identical APPJ without shielding gas.

Figure 8 shows simulated and experimental radial distributions of the mole fraction of oxygen, nitrogen, and argon, at axial distances of 1 mm, 3 mm, and 5 mm from the nozzle, with and without shielding gas. In general, the simulated mole fractions are larger than the measured values. For all three axial locations, both simulations and experiments show that in the presence of nitrogen shielding gas, the mole fractions of oxygen and argon decrease while the mole fraction of nitrogen increases in accordance with expectation. The simulated mole fractions of all air components minimize at the centerline and increase monotonically along the radius. While both the measured and simulated mole fraction radial profiles become less center-low with increasing axial distance from the nozzle, the experimental  $O_2$  and  $Ar$  profiles dip no more than 2-fold over the  $\pm 0.5$  mm distance included in the Abel inversion at 3 mm and 5 mm axial distance, and measured  $N_2$  mole fractions actually peak slightly at the center. Simulations predict that the mole fractions fall about 9-fold and 3-fold from the edge to the center at 3 mm and 5 mm axial distance, respectively.

Simulations would be expected to reproduce the correct  $Ar:O_2:N_2$  ratio of air in the absence of shielding gas, since the diffusivity of these species in an air/He mixture are quite similar. The measured air composition is much closer to simulation predictions for larger distances from the nozzle (i.e. 5 mm). As discussed above, small mole fractions ( $\sim 10^{-5}$ ) of  $Ar$  and oxygen-containing ( $H_2O$ ,  $O_2$ ) impurities in the He carrier gas leads to levels of  $Ar$  and  $O_2$  higher than that possible

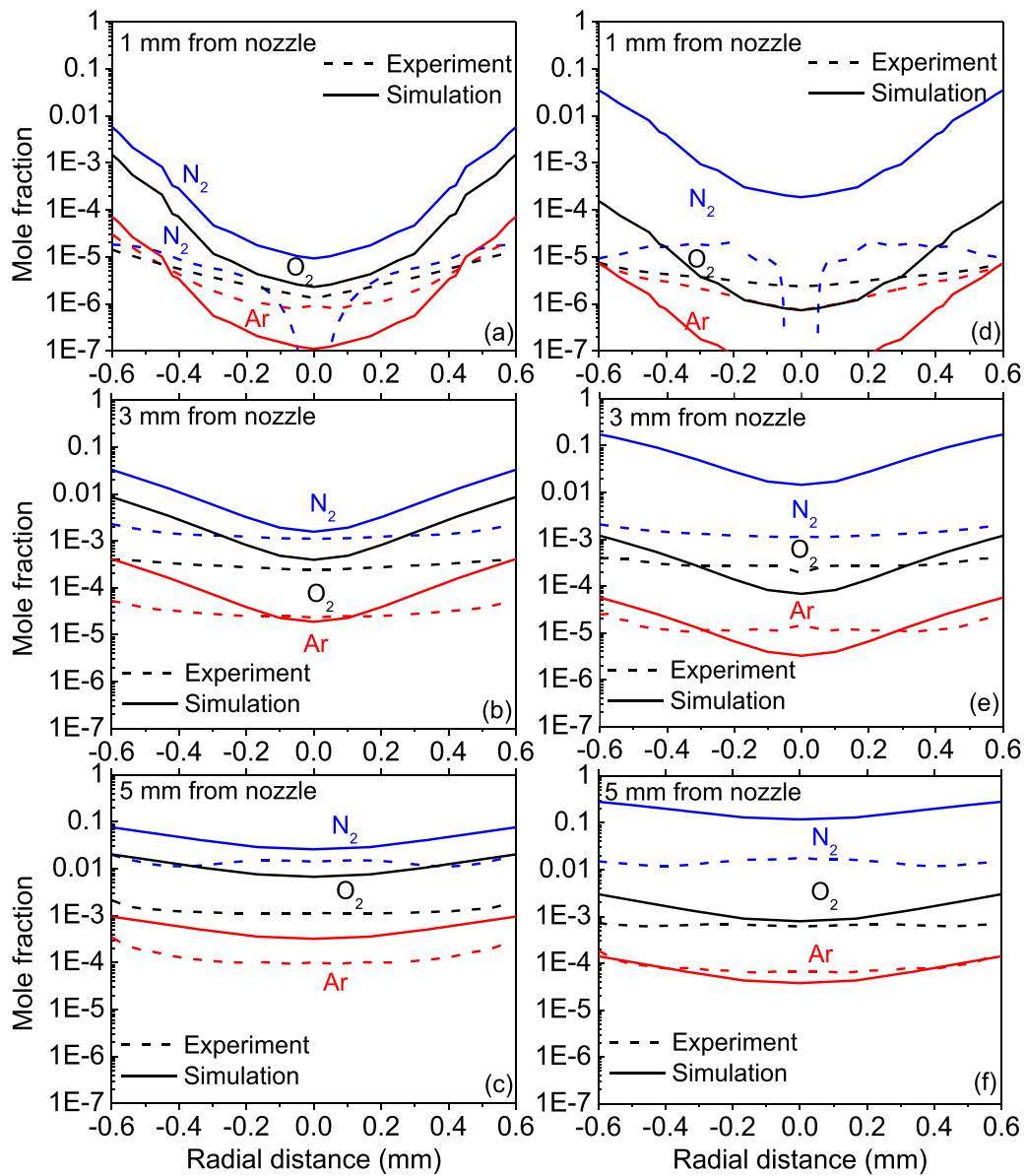


**Figure 8.** Mole fraction radial profiles of  $O_2$ ,  $N_2$  and Ar at axial distances from the nozzle of 1 mm, 3 mm, and 5 mm, without (a)–(c), and with (d)–(f) shielding gas. Solid lines are simulation predictions, broken lines are experimental profiles.

for air (i.e. relative to  $N_2$ ) at 3 mm and especially 1 mm from the nozzle, as well as a flatter profile than predicted by simulations. Also, the experimental uncertainty is higher in measuring such low mole fractions.

At the radial position  $r = 0.45$  mm ( $\sim$  the edge of the plasma column), the measured nitrogen mole fraction increases by a factor of 100, going from 1 mm to 3 mm from the nozzle, and by a factor of 10 going from 3 mm to 5 mm from the nozzle, both with and without shielding gas. The simulation predicts a similar relative increase in  $N_2$  at this radial position without shielding gas. With shielding gas the simulated  $N_2$  mole fractions at the radial edge increase dramatically and become less dependent on axial position than do the measured values. An increase of nitrogen mole fraction with nitrogen shielding gas could be attributed to enhanced mass

transport due to the stronger convective flow in the presence of shielding gas. It should be pointed out, however, that the raw OES measurement of  $N_2$ -to-He emission (before the Abel inversion) is virtually unchanged (0.3% decrease) in the presence of shielding gas, while the simulated  $N_2$  mole fraction near the axial center (where the raw OES measurements are most heavily weighted toward) increases  $\sim 3$ – $30$  times as a function of decreasing axial distance from the nozzle. The reason for this discrepancy between simulations and measurements is not clear.

Clearer comparisons between simulation predictions and experimental data in figure 8 of the on-axis mole fraction of  $O_2$ ,  $N_2$  and Ar at different distances from the nozzle, without shielding gas, are shown in figure 9. The mole fraction of nitrogen at a distance from the nozzle of 1 mm is too low to be

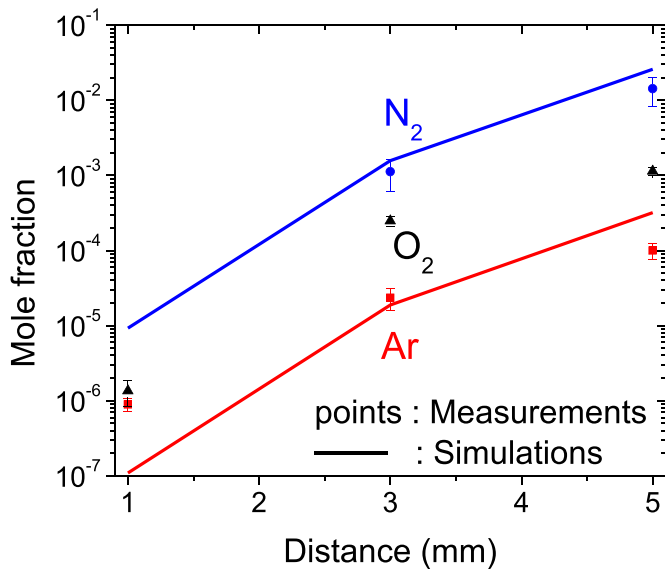


**Figure 9.** Comparison between simulation predictions (lines) to experimental data (points) of the on-axis mole fraction of  $O_2$ ,  $N_2$  and Ar for three axial distances from the nozzle, without shielding gas.

measured, so its experimental point is missing. At 3 mm from the nozzle, the simulated oxygen and argon mole fractions are in good agreement with experimental data. At 5 mm, the agreement is reasonable, except for  $O_2$ , where the simulation predicts about 6 times higher mole fractions. Close to the nozzle (i.e. 1 mm), the measured Ar mole fraction is 9 times higher than the simulations. As discussed above, the too-high Ar levels at this position were caused by a trace Ar impurity in the helium feed gas. The simulation did not account for such impurities. In addition, for all three species, the mole fraction ratio between 3 mm and 1 mm from the nozzle is much higher than the corresponding ratio between 5 mm and 3 mm from the nozzle, which agrees with the experimental trend.

The discrepancy between measured and simulated radial number density profiles could be due to an assumption made in the actinometric method. The actinometric calibrations were performed without shielding gas using line-integrated emission across the plasma radius, perpendicular to and passing through the central axis. Thus, it was assumed that the excitation rate constants for Ar,  $N_2$ , He and  $He^*$  as well as the emission yields of excited species each were affected to the same degree at all radial positions, with or without shielding gas. Nevertheless, overall, the simulation captures the salient features of the experimental measurements.

### 3.6. Comparison with published literature

The effect of shielding gas on an APPJ has been studied before, especially on the commercial device named kINPen [19, 58]. The shielding gas was found to be very effective, reducing air diffusion at 5 mm from the nozzle by 5–10 times [10, 59], compared to the 2–4 times air diffusion reduction measured

in this study. This discrepancy can be explained by the high power applied to the plasma jet, resulting in higher gas temperature. The plasma jet in the present study was operated with 40 W nominal power, producing a gas temperature of  $\sim 900$  K. On the other hand, the kINPen was operated with less than 3.5 W, resulting in a gas temperature less than 320 K [58]. Higher temperature leads to higher diffusivity, thus lowering the effectiveness of shielding gas. To ascertain this hypothesis, simulation of air diffusion was also ran with 300 K, instead of the simulated gas temperature of 800 K–1200 K, to observe the impact of diffusivity on shielding gas effectiveness. Compared to the high temperature simulation, which resulted in shielding gas reduction of air diffusion by roughly ten-fold, the 300 K simulation showed shielding gas reducing air diffusion by  $\sim 100$  times, proving that the shielding gas becomes less effective with high gas temperature, though in both cases, simulations predict a larger effectiveness in shielding gas than was found experimentally. Therefore, the low effectiveness of shielding gas seen in this study compared to others can be attributed to the higher gas temperature of the APPJ studied in the present work.

The results in the present study (without shielding gas) can also be compared with Raman scattering measurements of air diffusing into an APPJ with a feed gas of Ar and 2% air, reported by van Gessel *et al* for a similar discharge configuration [60]. The presence of 2% air in the feed gas make it difficult to compare their study to the present case. At large radial and axial distances, however, the feed gas is not the main source of air, hence valid comparisons can be made. At axial distances of 1, 3 and 5 mm, they found respective air mole fractions of 0.2, 0.25, and 0.4 at the edge (6 mm radial distance) of the jet, compared with measured (simulated) values of 0.00002 (0.007), 0.002 (0.03), and 0.02 (0.09) at these respective positions in the present study (see figures 7(b) and 8(b)). Since the study of van Gessel *et al* was of an Ar plasma at lower power (3.5 W) and hence lower gas temperature (382 K), one would expect slower diffusion and lower air levels diffusing into the plasma from the surrounding ambient.

The disagreement among the experimental and modeling studies summarized here is likely due to differences in plasma operation, especially power densities.

## 4. Summary and conclusions

The radial mole fraction profiles of air species diffusing into a radio frequency, APPJ, with 2 slm helium flow were determined by means of optical emission spectroscopy. The probed emissions were transformed into radial emission profiles by Abel inversion, then converted into mole fraction profiles via self-actinometry, using results from a set of calibrations. Self-actinometry involves adding a trace amount of the species of interest (Ar,  $O_2$ , or  $N_2$ ) to the feed gas flow and observing the respective relative change in Ar,  $O_2$ , and  $N_2$  emission intensity. Proper corrections due to quenching of the excited

states by added trace gases were applied. Experimental results showed that the air mole fraction increased along the axis of the He jet from essentially zero at 1 mm, to  $10^{-3}$  at 3 mm, to  $10^{-2}$  at 5 mm axial distance from the nozzle. Radial species distributions started out center-low at 1 mm, but became mostly flat at 5 mm from the nozzle. Further, it was found that the Ar, O<sub>2</sub>, and N<sub>2</sub> mole fractions matched the air composition at 3 mm and 5 mm from the nozzle, accounting for experimental error. Experimental data were compared to the predictions of a simulation combining a neutral fluid flow, heat and mass transport model, with a plasma dynamics model. Overall, the simulation captured the main features of the species concentrations and their profiles. It was concluded that this self-actinometry method can provide accurate absolute number density of plasma species, even at atmospheric pressure.

The addition of 4.5 slm N<sub>2</sub> shielding gas flowing co-axially and engulfing the He jet, reduced ambient air diffusion by 2–4 times. The shielding gas effectiveness in this study was lower than previously reported [10, 59] (up to more than 10 times reduction in air diffusion). This was attributed to the high operating power (nominal power of 40 W) of the plasma source in this work, leading to higher gas temperature ( $\sim 900$  K), compared to the lower power (3.5 W) and lower gas temperature (320 K) of the kINPen plasma source used in the other studies [58].

### Data availability statement

All data that support the findings of this study are included within the article (and any supplementary files).

### Acknowledgments

The authors are grateful to the Department of Energy (Office of Fusion Energy Science, contract No. DE-SC0001939) for financial support of this work.

### Appendix

Measured on-axis He emission intensities at axial distances of 1 mm and 5 mm from the nozzle were compared with the model predictions [57]. He emission intensities computed with no additional N<sub>2</sub>, and with an addition of 0.0002 mole fraction are given by the lines in figure A1. At 1 mm and 5 mm from the nozzle, the N<sub>2</sub> mole fractions from in-diffusing air were computed to be  $9.3 \times 10^{-6}$  and 0.026. The measurements in figure 3 at axial distances of 1 mm and 5 mm are reproduced in figure A1. At both axial distances the model agrees well with the experimental measurements in that there is only a small change in He emission intensity induced by the addition of a small amount of N<sub>2</sub>. This further justifies the application of the self-actinometry method to obtain quantitative number densities from optical emission under the extreme conditions in atmospheric pressure plasmas.

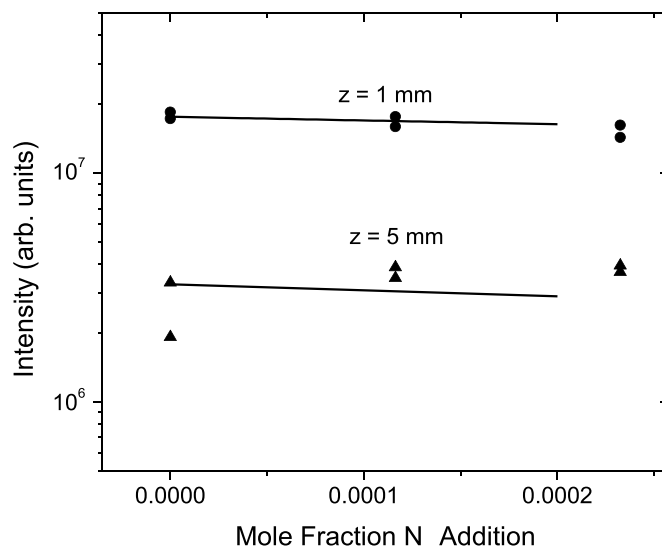


**Figure A1.** Model predictions (solid lines) of on-axis He emission intensity (706 nm) at 1 mm and 5 mm axial distance from the nozzle, as a function of N<sub>2</sub> addition to the He feed gas flow. At 1 mm and 5 mm from the nozzle, the N<sub>2</sub> mole fractions from in-diffusing air were computed to be  $9.3 \times 10^{-6}$  and 0.026 with zero mole fraction added N<sub>2</sub>. The points are the experimental measurements in figure 4.

### ORCID iD

Vincent M Donnelly  <https://orcid.org/0000-0001-5834-6678>

### References

- [1] Tendero C, Tixier C, Tristant P, Desmaison J and Leprince P 2006 *Spectrochim. Acta B* **61** 2
- [2] Penkov O V, Khadem M, Lim W S and Kim D E 2015 *J. Coat. Technol. Res.* **12** 225
- [3] Mariotti D and Sankaran R M 2010 *J. Phys. D: Appl. Phys.* **43** 323001
- [4] Schütze A, Jeong J Y, Babayan S E, Park J, Selwyn G S and Hicks R F 1998 *IEEE Trans. Plasma Sci.* **26** 1685
- [5] Lu X, Laroussi M and Puech V 2012 *Plasma Sources Sci. Technol.* **21** 034005
- [6] Ehlbeck J, Schnabel U, Polak M, Winter J, Von Woedtke T, Brandenburg R, Von Dem Hagen T and Weltmann K D 2011 *J. Phys. D: Appl. Phys.* **44** 13002
- [7] Sousa J S, Niemi K, Cox L J, Algwari Q T, Gans T and O'Connell D 2011 *J. Appl. Phys.* **109** 123302
- [8] Ito T, Uchida G, Nakajima A, Takenaka K and Setsuhara Y 2017 *Japan. J. Appl. Phys.* **56** 01AC06
- [9] Iseni S, Zhang S, Van Gessel A F H, Hofmann S, Van Ham B T J, Reuter S, Weltmann K D and Bruggeman P J 2014 *New J. Phys.* **16** 123011
- [10] Reuter S, Winter J, Schmidt-Bleker A, Tresp H, Hammer M U and Weltmann K D 2012 *IEEE Trans. Plasma Sci.* **40** 2788
- [11] Dünbnier M, Schmidt-Bleker A, Winter J, Wolfram M, Hippler R, Weltmann K D and Reuter S 2013 *J. Phys. D: Appl. Phys.* **46** 435203
- [12] Schmidt-Bleker A, Winter J, Bösel A, Reuter S and Weltmann K D 2015 *Plasma Sources Sci. Technol.* **25** 015005

- [13] Schmidt-Bleker A, Winter J, Iseni S, Dünnbier M, Weltmann K D and Reuter S 2014 *J. Phys. D: Appl. Phys.* **47** 145201
- [14] Reuter S, Tresp H, Wende K, Hammer M U, Winter J, Masur K, Schmidt-Bleker A and Weltmann K D 2012 *IEEE Trans. Plasma Sci.* **40** 2986
- [15] Narimisa M, Onyshchenko Y, Morent R and De Geyter N 2021 *Polymer* **215** 123421
- [16] Kapaldo J, Han X and Ptasincka S 2019 *Plasma Process. Polym.* **16** 1
- [17] Ogawa K, Yajima H, Oh J S, Furuta H and Hatta A 2019 *Appl. Phys. Express* **12** 036001
- [18] Schmidt-Bleker A, Norberg S A, Winter J, Johnsen E, Reuter S, Weltmann K D and Kushner M J 2015 *Plasma Sources Sci. Technol.* **24** 035022
- [19] Reuter S, Von Woedtke T and Weltmann K D 2018 *J. Phys. D: Appl. Phys.* **51** 233001
- [20] Waskoenig J, Niemi K, Knake N, Graham L M, Reuter S, Schulz-Von Der Gathen V and Gans T 2010 *Plasma Sources Sci. Technol.* **19** 045018
- [21] Pei X, Wu S, Xian Y, Lu X and Pan Y 2014 *IEEE Trans. Plasma Sci.* **42** 1206
- [22] Xiong Q, Yang Z and Bruggeman P J 2015 *J. Phys. D: Appl. Phys.* **48** 424008
- [23] Van Gessel A F H, Alards K M J and Bruggeman P J 2013 *J. Phys. D: Appl. Phys.* **46** 265202
- [24] Pipa A V, Bindemann T, Foest R, Kindel E, Röpcke J and Weltmann K D 2008 *J. Phys. D: Appl. Phys.* **41** 194011
- [25] Kaminski C F, Löfstedt B, Fritzon R and Aldén M 1996 *Opt. Commun.* **129** 38
- [26] McCann M P, Chen C H and Payne M G 1988 *J. Chem. Phys.* **89** 5429
- [27] Lempert W R and Adamovich I V 2014 *J. Phys. D: Appl. Phys.* **47** 433001
- [28] Kang S J and Donnelly V M 2007 *Plasma Sources Sci. Technol.* **16** 265
- [29] Karakas E, Kaler S, Lou Q, Donnelly V M and Economou D J 2014 *J. Phys. D: Appl. Phys.* **47** 085203
- [30] Seitz C A 1984 *Bur. Mines Rep. Invest.* **8941** 8914
- [31] Hofmann S, Van Gessel A F H, Verreycken T and Bruggeman P 2011 *Plasma Sources Sci. Technol.* **20** 65010
- [32] Wang Q, Koleva I, Donnelly V M and Economou D J 2005 *J. Phys. D: Appl. Phys.* **38** 1690
- [33] Wang Q, Doll F, Donnelly V M, Economou D J, Sadeghi N and Franz G F 2007 *J. Phys. D: Appl. Phys.* **40** 4202
- [34] Nguyen T 2020 PhD Dissertation University of Houston
- [35] Nguyen T, Hernandez E, Donnelly V M and Economou D J 2018 *J. Vac. Sci. Technol. A* **36** 04F406
- [36] Xiong Q et al 2009 *J. Appl. Phys.* **106** 83302
- [37] Zhu W C, Li Q, Zhu X M and Pu Y K 2009 *J. Phys. D: Appl. Phys.* **42** 202002
- [38] De Heer F J 1998 He cross sections compilation
- [39] Wiese W L, Brault J W, Danzmann K, Helbig V and Kock M 1989 *Phys. Rev. A* **39** 2461
- [40] Sadeghi N, Setser D W, Francis A, Czarnetzki U and Döbele H F 2001 *J. Chem. Phys.* **115** 3144
- [41] Drake G 2006 *Springer Handb. At. Mol. Opt. Phys.* (New York: Springer-Verlag)
- [42] Frost M J, Himmelmann S and Palmer D D 2001 *J. Phys. B: At. Mol. Opt. Phys.* **34** 1569
- [43] Hitachi A, King T A, Kubota S and Doke T 1980 *Phys. Rev. A* **22** 863
- [44] Hibbert A, Biémont E, Godefroid M and Vaeck N 1991 *J. Phys. B: At. Mol. Opt. Phys.* **24** 3943
- [45] Liu X Y, Hu J T, Liu J H, Xiong Z L, Liu D W, Lu X P and Shi J J 2012 *Appl. Phys. Lett.* **101** 43705
- [46] Pagnon D, Amorim J, Nahorny J, Touzeau M and Vialle M 1995 *J. Phys. D: Appl. Phys.* **28** 1856
- [47] Bittner J, Kohse-höinghaus K, Meier U and Just T 1988 *Chem. Phys. Lett.* **143** 571
- [48] Huber K P and Herzberg G 1979 *Molecular Spectra and Molecular Structure* (lancaster: lancaster press, inc)
- [49] Gat E, Gherardi N, Lemoing S, Massines F and Ricard A 1999 *Chem. Phys. Lett.* **306** 253
- [50] Puech V, Collier F and Cottin P 1977 *J. Chem. Phys.* **67** 2887
- [51] Valk F, Aints M, Paris P, Plank T, Maksimov J and Tamm A 2010 *J. Phys. D: Appl. Phys.* **43** 385202
- [52] Lepikhin N D, Klochko A V, Popov N A and Starikovskaia S M 2016 *Plasma Sources Sci. Technol.* **25** 45003
- [53] Phelps A V 1955 *Phys. Rev.* **99** 1307
- [54] Lindinger W, Schmeltekopf A L and Fehsenfeld F C 1974 *J. Chem. Phys.* **61** 2890–5
- [55] Myers G and Cunningham A J 1977 *J. Chem. Phys.* **67** 3352
- [56] Emmert F, Angermann H H, Dux R and Langhoff H 1988 *J. Phys. D: Appl. Phys.* **21** 667
- [57] Lin P, Zhang J, Nguyen T, Donnelly V M and Economou D J 2021 *J. Appl. Phys.* **54** 075205
- [58] Bekeschus S, Schmidt A, Weltmann K D and Von Woedtke T 2016 *Clin. Plasma Med.* **4** 19
- [59] Jablonowski H, Hänsch M A C, Dünnbier M, Wende K, Hammer M U, Weltmann K-D, Reuter S and Von Woedtke T 2015 *Biointerphases* **10** 029506
- [60] Van Gessel B, Brandenburg R and Bruggeman P 2013 *Appl. Phys. Lett.* **103** 064103